Lattice and beam dynamics for the pulse mode of the laser-electron storage ring for a Compton x-ray source

Peicheng Yu,* Yu Wang, and Wenhui Huang

Accelerator Laboratory, Department of Engineering Physics, Tsinghua University, Beijing 100084, China, and Key Laboratory of Particle and Radiation Imaging of Ministry of Education, Tsinghua University, Beijing 100084, China

(Received 5 September 2008; published 9 June 2009)

We present the lattice design for the pulse mode of the compact laser-electron storage ring for a Compton x-ray source. The lattice is optimized to suppress the intrabeam scattering (IBS), which is the dominant factor that leads to emittance growth. To better simulate the beam dynamics in the pulse mode, we developed a macroparticle 3D Monte Carlo algorithm. The IBS module can perform an element-to-element calculation to evaluate the emittance change due to IBS, while the Compton scattering module can provide the spatial and temporal information of the x-ray photon yield. Parameters of the storage ring, electron beam, and scattered photon yield of the pulse mode of this Compton x-ray source are presented.

DOI: 10.1103/PhysRevSTAB.12.061301 PACS numbers: 41.60.−m, 29.27.Bd, 29.20.D−

I. INTRODUCTION

Compton scattering (CS) off a relativistic electron beam with an intense laser pulse is a promising way of producing x ray with high intensity. The idea of utilizing a laser-electron storage ring (LESR) for the purpose of increasing frequency and luminosity of x ray by means of CS was proposed by Huang and Ruth in 1998 [1]. The basic principle of this scheme is the Compton scattering off a low-energy electron beam stored in a storage ring with an intense laser pulse stored in an optical storage system to produce the desired photon spectrum. In a head-on collision, the maximal scattered photon energy can be represented by $E_{x,\max} = 4\gamma^2 E_{\mathrm{las}}$, where γ is the relative energy of the electron and E_{las} is the laser photon energy. The micropulse of the scattered photon is about the same length as that of the electron beam. For instance, with a 50 MeV, 10 ps electron beam scattering off laser photons with the energy $E_{\mathrm{las}} = 1.467$ eV, one can produce an x-ray pulse with a photon energy of $E_{x,\max} = 56.4$ keV and a pulse length of 10 ps (head-on collision). Because of its compactness and low construction cost, this scheme is a competitive proposal to generate high intensity x-ray photons.

There are two main schemes for the LESR operation. One is the steady mode of operation, in which the electron beam is stored in the ring for a long period of time and the equilibrium parameters of the electron beam are achieved [2]. The ring is designed to have a controlled momentum compaction factor, which enables the ring to keep a long-term stable motion of electron beam with a large energy spread owing to CS. The x-ray photon yield is stable because of the utilization of the steady-state electron beam.

The other scheme is the pulse mode of operation [3]. In this mode, the electron beam is injected and stored for a short period of time (we call it the storage period) during which electron beam interacts with the laser photons. The frequency of the injection and dumping is 50–60 Hz, hence the beam is dumped long before the equilibrium parameters are achieved. Owing to the strong intrabeam scattering (IBS) effect, the emittance of the beam increases quite rapidly, and the intensity of the scattered photon decreases within a relatively short period. Hence, the pulse mode takes advantage of the initial parameters of the electron beam to enhance its average intensity. Therefore, the x-ray source based on this scheme can be utilized in technological and scientific applications requiring high intensity and pulse nature of the x ray.

In this paper, we proposed a lattice design for the pulse mode of the laser-electron storage ring to store the electron beam and provide stable interaction between the electron and the laser photon. We utilized an intense, low emittance photocathode rf injector to be the electron source, in order that the beam parameters right after the injection are much better than the equilibrium parameters determined by the storage ring. Since the damping time of the storage ring owing to synchrotron radiation (SR) and CS is about the order of one second, the energy distribution of the beam right before the dumping is much closer to the initial distribution.

The main dynamic features of the pulse mode involve IBS and CS. In the pulse mode, IBS is the dominant factor for the emittance growth. Since the storage time of the electron beam in the ring is relatively short, we adopted a macroparticle algorithm originated from the binary collision model [4] to simulate the IBS effect. The algorithm can be utilized for particle beam with arbitrary distribution. Furthermore, in order to obtain the spatial and temporal distribution of the x-ray photon yield in the storage period, we adopted a 3D Monte Carlo simulation algorithm to simulate the effect of CS on the beam dynamics.

Owing to the small bending radius of the ring, short beam length and large charge quantity of the electron

*tpc02@mails.thu.edu.cn

beam, coherent synchrotron radiation (CSR) likewise becomes significant. Recent work [5] has shown that CSR can alone account for the beam instability in such a compact storage ring. Following the approaches in Refs. [5,6], we evaluated the CSR threshold for the pulse mode of the LESR.

The remainder of this paper is organized as follows: Sec. II discusses the LESR lattice. In Sec. III, we focus on the dynamic features of the LESR and the simulation method. Section IV presents the parameters of the electron beam and scattered photon. The conclusions and discussions are summarized in Sec. V.

II. LATTICE DESIGN OF THE LESR

A. Intrabeam scattering

The emittance growth caused by the IBS is quite large at the energy range of 20–80 MeV. As we can see from the simulation result of our original optics design [7] (see Fig. 6), the transverse emittance grows 13 times in the storage period. The IBS effect contributes to the majority of the emittance growth. Hence, suppressing the IBS in the optics design can benefit the total yield of the x-ray photon and stability of the electron beam.

The correlation between transverse and longitudinal IBS diffusion coefficients $d\epsilon_x/ds = \frac{1}{2}\mathcal{H}_x d\sigma_\delta^2/ds$ makes it possible to reduce the horizontal IBS growth rate by reducing the $\mathcal{H}_x$ function [8,9], where

$$\mathcal{H}_x = \gamma_x D_x^2 + 2\alpha_x D_x D_x' + \beta_x D_x'^2, \tag{1}$$

α_x, β_x, and γ_x are the Twiss function of the lattice, and D_x and D_x' are the dispersion function. From another point of view, the majority of the horizontal emittance growth is attributable to the coupling in the arc area, in which the longitudinal momentum changes couple into the horizontal direction. The horizontal invariant change caused by the longitudinal momentum change can be expressed by

$$dJ_x = \frac{2\Delta P_s}{P}[\alpha_x(D_x' x_\beta + D_x x_\beta') + D_x \gamma_x x_\beta + \beta_x D_x' x_\beta'] + \left(\frac{\Delta P_s}{P}\right)^2 \mathcal{H}_x, \tag{2}$$

where $\Delta P_s/P$ is the relative longitudinal momentum change, and x_β and x_β' are the betatron amplitude of the electron and its deviation. Since the transverse phase space of the electron beam is usually symmetric, the second term in Eq. (2) contributes to most of the horizontal emittance growth. For the same lattice, we compared the IBS growth rate among three optics, as presented in Table I and Fig. 6. As we can see in Table I, the average value of $\langle \mathcal{H}_x \rangle$ is the largest for the steady mode optics [10], which results in the largest IBS growth rate in the horizontal direction.

We should keep the space charge tune shift small to prevent beam loss. Taking the horizontal direction, for instance, the space charge incoherent tune shift around the ring can be expressed by [1,11]

$$\Delta \nu_x = -\frac{N_e r_0 \rho}{\sqrt{2\pi}\gamma^3 \sigma_s} \frac{1}{(\epsilon_x + \frac{D_x^2 \sigma_\delta^2}{\beta_x}) + \sqrt{(\epsilon_x + \frac{D_x^2 \sigma_\delta^2}{\beta_x})\epsilon_y \frac{\beta_y}{\beta_x}}}, \tag{3}$$

where N_e is the number of electrons in the bunch, $r_0 = 2.85 \times 10^{-15}$ m is the classical radius of the electron, σ_s is the beam length, σ_δ is the relative energy spread, and ρ is the average ring radius.

As evident in Eq. (3), we can control the tune shift by increasing the transverse emittance and reducing the values of the beta function. Although emittance growth owing to IBS (cf. Fig. 6) can control the tune shift in the storage period, a low average value of the beta function can minimize the tune shift in the first place.

Based upon the optics we proposed in [7] (we name it the original optics), we accomplished the IBS suppression by increasing the strength of the quadrupoles all over the ring. As a result, we increased the betatron tune and reduced the values of the $\mathcal{H}_x$ and beta function (we name the new optics the IBS-suppression optics). Compared with the original optics, we successfully reduced the average value of $\mathcal{H}_x$ by 10% with the IBS-suppression optics, and shifted the working point from $(Q_x, Q_y) = (2.78, 1.61)$ to $(Q_x, Q_y) = (2.87, 1.69)$. The emittance growth rate for the IBS-suppression optics and the original optics are presented in Fig. 6 and Table I. As evident in Table I, the former achieves 25% reduction in the IBS growth rate.

Nevertheless, in spite of the IBS suppression, the emittance grows rapidly in a relatively short period of time. This problem is quite difficult to solve using the state-of-the-art technique when electron energy is in the range of 20–80 MeV. The optics with IBS suppression can partly

TABLE I. Average values of Twiss functions and IBS growth rate for different optics.

Parameters	IBS-suppression optics	Original optics	Steady mode optics
$\bar{\mathcal{H}}_x$	0.086	0.098	0.401
$\bar{\beta}_x$	1.728	2.74	1.58
$\langle D_x^2 \rangle$	0.122	0.121	0.179
Tune (Q_x, Q_y)	(2.87, 1.69)	(2.78, 1.61)	(3.19, 1.66)
ϵ_x (at 4×10^5 turn), m	2.25×10^{-7}	2.8×10^{-7}	4.7×10^{-7}

decrease the strength of IBS, yet this method is limited by the maximum strength of the quadrupoles and the lattice requirements of the LESR, which set constraints on the quadrupoles strength [8]. Hence, utilizing a low-energy electron beam and adopting the pulse mode of the LESR can inevitably generate x ray with pulse nature.

B. Main requirements of the LESR ring lattice

Since we chose to operate the storage ring in the pulse mode, the main requirements of the lattice design were to minimize the beam size at the interaction point (IP) to achieve high intensity of the scattered photon. With respect to the transverse beam size, we had to minimize the beta function at the IP. We placed quadrupole quadruplets to achieve low beta insertion at the IP. However, the strong quadrupoles brought large natural chromaticity to the ring, which should be suppressed by the sextupoles in the dispersive area. As a result, the dynamic aperture (DA) greatly decreased. Thus, we had to place harmonic sextupoles in the dispersion-free long straight section to reduce the resonance-driven terms in the Hamiltonian to enhance the DA.

The dispersion function at the section in which we placed the IP not only contributes to the transverse beam size, but also contributes to the emittance growth because of the CS. It is evident from Eq. (1) and (2) that, if $D_x = 0$ and $D_x' = 0$ at the IP, the contribution from the longitudinal momentum change can be eliminated. Otherwise, the longitudinal momentum change can result in a shift in the closed orbit, and thus increases the horizontal invariant of the electron, which is quite similar to the case in synchrotron radiation. Hence, the dispersion function at the IP should be zero. Likewise, the dispersion function should be zero at the place where we positioned the rf cavity and injection system to ensure beam stability.

Hence, the lattice of the LESR should meet the following requirements: (i) The beta function at the interaction point should be small to focus the electron beam to a small size to enhance the yield of the scattered photon. (ii) The dispersion at the point where IP, rf cavity, and injection system are placed should be zero to ensure beam stability. (iii) The large natural chromaticity at the IP has to be compensated by groups of sextupoles placed in the arc area. As a result, harmonic sextupoles should be placed into the long straight section to enhance the DA. (iv) $\bar{\mathcal{H}}_x$ should be optimized to minimize the IBS effect.

C. Layout of the ring lattice

The layout of the lattice is presented in Fig. 1. The racetrack design [2,3] is adequate for the requirements mentioned above. The DBA structure ensures two long straight sections with zero dispersion. We placed the IP at the position with a low beta insertion. On the opposite side, we placed the injection system in one of the long drifts. Groups of quadrupoles are placed in the middle of the long straight section to make the lattice more flexible. These groups of quadrupoles are crucial for IBS suppression. Moreover, they make the dispersion function in this section more flexible, which is important if we want to change the momentum compaction factor and operate the ring in the steady mode [2]. Two groups of sextupoles are placed in the arc area to correct the chromaticity, and groups of harmonic sextupoles are placed at both long straight sections to enhance the DA.

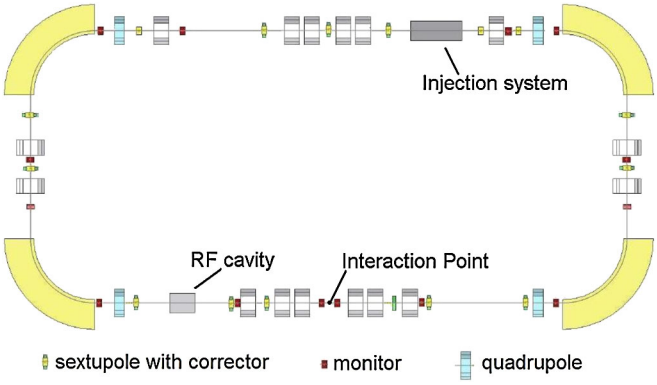

FIG. 1. (Color) Layout of the ring lattice. The DBA structure provides two long straight sections that are dispersion-free. The IP and the rf cavity are placed at the lower straight section, while the injection system is placed at the upper one.

The Twiss function is presented in Fig. 2. The circumference of the ring is 11.918 m. The beta function at the IP is $\beta_x = 0.049$ m and $\beta_y = 0.115$ m. The first order dispersion D_{1x} at the IP is zero, while the second order dispersion is $D_{2x} = 0.21$ m. Considering that the energy spread of the beam does not exceed 0.3% when the beam is

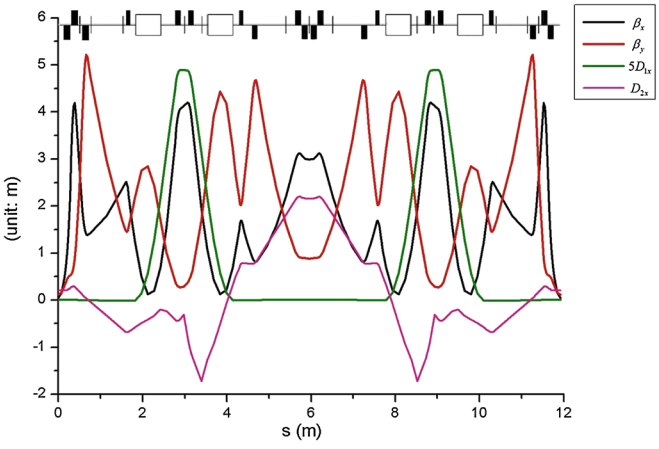

FIG. 2. (Color) Twiss functions of the ring lattice. The beta function at the IP is $\beta_x = 0.049$ m and $\beta_y = 0.115$ m. The first order dispersion at the IP is zero, while the second order dispersion is $D_{2x} = 0.21$ m, which is relatively small. We strengthened the quadrupoles to achieve higher betatron phase advance, which reduces the average value of the $\mathcal{H}_x$ function thus decreasing the IBS growth rate.

TABLE II. Parameters of the laser-electron storage ring.

Parameters	Values
Circumference, m	11.918
Radius of the dipole, m	0.38
Beam current, mA	25
Tunes	
Horizontal	2.87
Vertical	1.69
Beta function at IP	
Horizontal, cm	4.9
Vertical, cm	11.5
Mean energy loss per turn	
Synchrotron radiation, eV	1.42
Compton scattering (laser energy 1 mJ), eV	0.23
rf voltage, kV	300
rf frequency, GHz	1.2
Harmonic number	48
Momentum compaction factor	0.081
Energy acceptance	3.4%
Injection frequency, Hz	50–60
Horizontal beam size at IP	
Right after injection, μm	31
Right before dumping, μm	105
Natural chromaticity	
Horizontal	−6.06
Vertical	−4.09

dumped, D_{2x} is small enough. The maximum length of the drifts is 0.75 m. The momentum compaction factor of the ring is $\alpha_c = 0.081$. The ring parameters are listed in Table II.

D. Dynamic aperture

We enhanced the DA by means of harmonic sextupoles successfully with the help of the OPA lattice design code [12]. The on-momentum DA is related to the injection efficiency, while the off-momentum DA is related closely to the Touschek lifetime. We tracked the particles for 50 000 turns with various momentum deviations without errors, and with errors (misalignments $\Delta x, y_{\mathrm{rms}} = 1 \times 10^{-4}$ m, tilts $\Delta\phi_{\mathrm{rms}} = 1 \times 10^{-4}$ rad, dipole field deviation 5×10^{-4}, and quadrupole field deviation 1×10^{-2}). The results are shown in Fig. 3(a). We likewise tracked the on-momentum frequency map [13] for 10 000 turns without errors [cf. Figs. 4(a) and 4(b)]. The frequency map presents the diffusion index of the tunes at the IP by a color scale which is utilized as an index of stability. We followed the definition in Ref. [13]; hence, a color spot below blue indicates a stable point with the tune diffusion less than 10^{-10}, while a color spot above red indicates a point with the tune diffusion greater than 10^{-2}, which is less stable. As we can see from Fig. 3(a), the on-momentum DA without errors is about 3 mm. However, the node between 5th-order resonance $\nu_x - 4\nu_y + 4 = 0$, 6th-order resonance $4\nu_x + 2\nu_y - 15 = 0$, and 7th-order resonance $5\nu_x - 2\nu_y - 11 = 0$ limits the DA [cf. Fig. 4(b)]. Moreover, the 4th-order resonance $\nu_x + 3\nu_y - 8 = 0$ causes chaotic motion at $x \approx \pm 2.1$ mm. We can see that when the 4th-order and 5th-order resonances are further excited by magnet errors, the DA would shrink to 2 mm [cf. Fig. 3(a)]. Nevertheless, since the maximum value of the horizontal beam size should not exceed 105 μm, the on-momentum DA is good enough for the pulse mode.

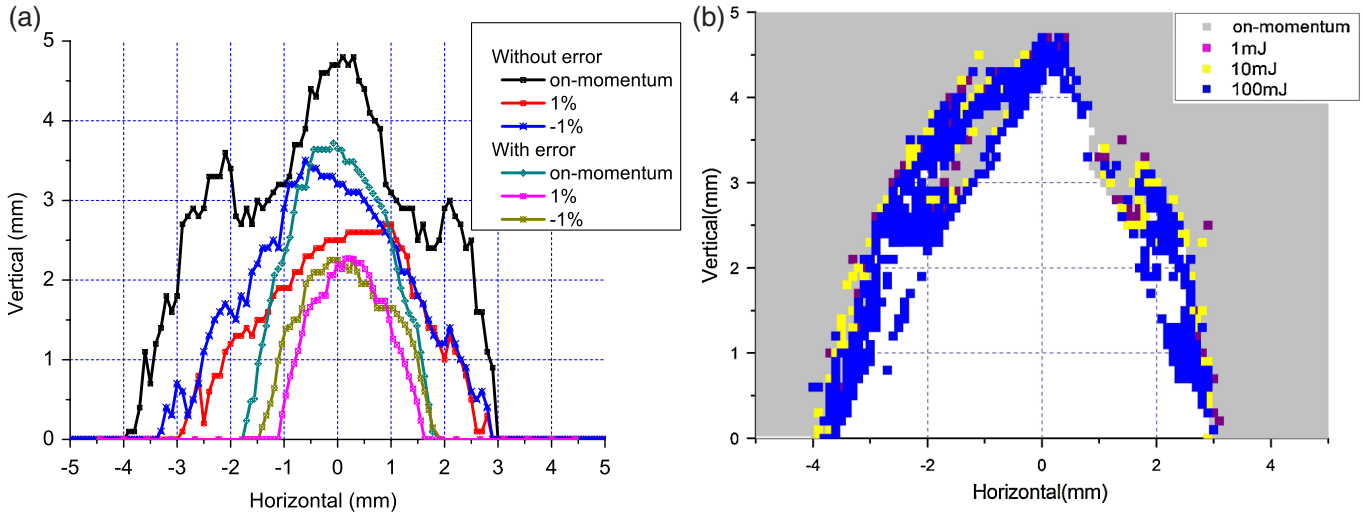

FIG. 3. (Color) Dynamic apertures for (a) various momentum deviations, and (b) various laser energies. The on-momentum DA without errors is about 3 mm. We tracked the particles for 50 000 turns with misalignments, tilts, and field errors included for various momentum deviations. The off-momentum DA at momentum deviation ±1% is about 1 mm. Even for the laser energy of 100 mJ, the DA is large enough for the stable motion of the electron. The dynamic aperture tracking including CS has shown that the lattice is robust enough for this stochastic process.

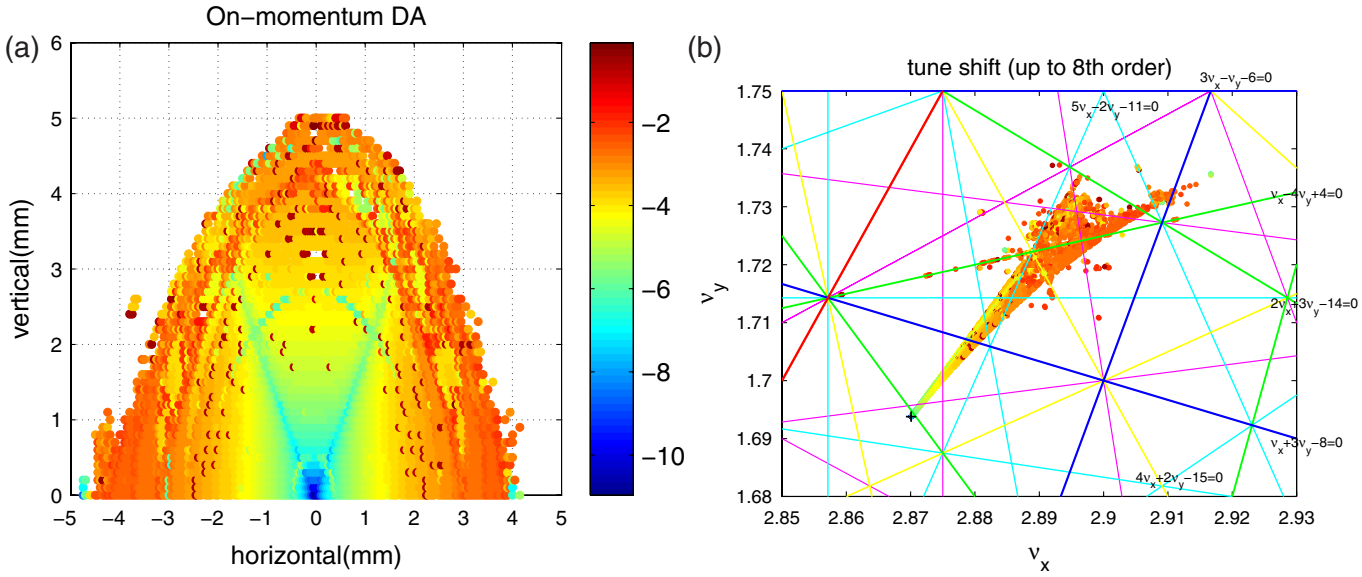

FIG. 4. (Color) (a) On-momentum DA and (b) the frequency map at the IP. Subfigure (a) presents the tune diffusion at the surface of the IP, while subfigure (b) presents the tune spread in the tune diagram. The point in the cooler color indicates that it has less tune diffusion, which is more stable. The dynamics is affected by the node between 5th-order resonance $\nu_x - 4\nu_y + 4 = 0$, 6th-order resonance $4\nu_x + 2\nu_y - 15 = 0$, and 7th-order resonance $5\nu_x - 2\nu_y - 11 = 0$. When the magnet errors further excite the 4th-order and 5th-order resonances, the DA would shrink to 2 mm.

The off-momentum DA is also important considering the strong IBS effect and the CS in this ring. Figure 3(a) shows that the DA at the momentum deviation of $\pm 1\%$ is still larger than 1 mm. Since CS is a stochastic process that renders large energy deviation to the electron beam, we accomplished a tracking with the CS included, and the result is shown in Fig. 3(b). As shown in the figure, when laser energy is below 100 mJ, the DA is quite sufficient. We did not include IBS in our simulation, owing to the fact that IBS is a collective effect that demands the parameters of the whole beam. Nevertheless, the tracking showed that the off-momentum DA is large enough for a beam with large energy deviation and stochastic process like the CS.

III. DYNAMIC FEATURES AND SIMULATION METHOD

The most important feature of the beam dynamics in the pulse mode of the LESR is the IBS, mainly caused by the low energy of the electron and the compactness of the storage ring. Another important factor is the CS. On one hand, the cross section of the CS is quite small (for the laser energy of 1 mJ stored in the optical cavity, the scattering chance for one electron per turn $\sim 2 \times 10^{-5}$); on the other hand, the energy of the scattered photon is relatively large. Therefore, CS can cause a large energy spread.

With respect to the synchrotron radiation (SR), owing to the low electron energy, the SR is not strong in this compact storage ring. The average number of the emitted photon per electron per turn due to SR is $\bar{N} = 6.48$, and the critical energy of the emitted photon is $u_c = 0.713$ eV. Nevertheless, we included SR in our simulation code.

The simulation is based upon the macroparticles algorithm. Each particle goes through the ring elements utilizing the transport matrix. After the beam passes through each lattice element, the IBS module is applied to calculate the electron momentum changes owing to IBS. Calculation of the IBS effect is accomplished by the binary collision model [4], in which macroparticles are paired and collided with one another with an equivalent scattering angle that renders the same emittance growth rate as that of the IBS. The CS module deals with the interactions between the particles and the laser photons. The code based on macroparticle algorithm is quite CPU-time consuming. Nevertheless, we only had to calculate the beam dynamics for the pulse mode, which means to track the particles for only 400 000 turns.

A. The binary collision algorithm for the intrabeam scattering

IBS is quite strong in the energy range of 20–80 MeV. The transverse emittance of the electron beam would grow rapidly owing to this effect, which results in the pulse nature of the x-ray photon yield in the pulse mode. To simulate the IBS growth in the pulse mode, we applied the binary collision model (BCM) [4] in our macroparticle simulation code. We will review the algorithm in the following paragraph.

The IBS simulation by BCM is based upon the approaches of Piwinski [14]. For two particles colliding with each other, the changes in momentum for particle 1 can be expressed as

$$\Delta P_{1x} = \frac{P}{2}\left[\zeta\sqrt{1+\frac{\xi^2}{4\alpha^2}}\sin\phi - \frac{\xi\theta}{2\alpha}\cos\phi\right]\sin\varphi + \theta(\cos\varphi - 1) \quad (4)$$

$$\Delta P_{1y} = \frac{P}{2}\left[\theta\sqrt{1+\frac{\xi^2}{4\alpha^2}}\sin\phi - \frac{\xi\zeta}{2\alpha}\cos\phi\right]\sin\varphi + \zeta(\cos\varphi - 1) \quad (5)$$

$$\Delta P_{1s} = \frac{P}{2}[2\alpha\gamma\sin\varphi\cos\phi + \gamma\xi(\cos\varphi - 1)], \quad (6)$$

where $\xi = \frac{P_1 - P_2}{\gamma P}$, $\theta = x_1' - x_2'$, $\zeta = y_1' - y_2'$, $\alpha = \frac{\sqrt{\theta^2+\zeta^2}}{2}$, φ and ϕ are the polar and azimuthal scattering angle correspondingly; P_1, P_2, x_1', x_2', y_1', and y_2' are the momentum and the slope of velocity in horizontal and vertical direction of the two particles, respectively; and P is the mean momentum of the two particles. Integrated over the scattering angle, the corresponding invariants change for particle 1 can be expressed by

$$\frac{dJ_{1x}}{dt} = \frac{\pi r_0^2}{4\gamma^2\bar{\beta}^3} c\rho L_c\left[-4x_1'\theta + \xi^2 + \zeta^2 + 4\frac{x_{\beta 1}D_x}{\beta_x^2}\gamma\xi + \frac{D_x^2\gamma^2}{\beta_x^2}(\theta^2+\zeta^2)\right] \quad (7)$$

$$\frac{dJ_{1y}}{dt} = \frac{\pi r_0^2}{4\gamma^2\bar{\beta}^3} c\rho L_c(-4y_1'\zeta + \xi^2 + \theta^2) \quad (8)$$

$$\frac{dJ_{1s}}{dt} = \frac{\pi r_0^2}{4\gamma^2\bar{\beta}^3} c\rho L_c\left(-4\frac{\delta_1}{\gamma}\xi + \zeta^2 + \theta^2\right), \quad (9)$$

where c is the speed of light, ρ is the electron density in the cell, L_c is the Coulomb logarithm, δ_1 is the momentum deviation for particle 1, and $\bar{\beta}$ is the average speed of the two particles.

The invariants growth rate owing to IBS can be evaluated by integrating Eqs. (7)–(9) over all the particles. This step is accomplished analytically for a Gaussian beam [14]. However, in our tracking code, the integration over the particles can be accomplished numerically, which makes the algorithm valid for an arbitrary distribution. Moreover, if we apply a discrete random process that causes the same invariants change as those indicated by Eqs. (7)–(9), the IBS growth rate can be evaluated by the equivalent collision process. The polar scattering angle of the equivalent collision process proposed by Alekseev [4] is

$$\varphi_{\text{eff}} = \frac{2r_0}{\gamma}\sqrt{\frac{\pi c\rho\Delta t_s}{\bar{\beta}^3}L_c}, \quad (10)$$

where $\Delta t_s = L_{\text{element}}/c$ is the time for the beam to pass the element. It is easy to verify that with the equivalent polar angle φ_{eff} and the azimuthal angle ϕ distributing uniformly in $[0, 2\pi]$, the invariant changes caused by the equivalent random process are the same as that of the IBS in the time interval Δt_s (see Appendix for details).

The IBS growth rate is evaluated in this way [4]: (i) The electron beam passes through an element of the lattice utilizing the transport matrix. (ii) The macroparticles are placed into different cells according to their positions in the space. (iii) The macroparticles in the same cells are paired randomly to collide with one another. The polar collision angles are calculated by Eq. (10), and the random azimuthal angles ϕ are generated uniformly in $[0, 2\pi]$. The momentum changes from the collisions are evaluated according to Eqs. (4)–(6). The electron density ρ is determined by the number of macroparticles in the cell. As a result, the invariant changes of all the macroparticles reveal the emittance change of the beam caused by the IBS in this element. (iv) Steps (i) to (iii) are repeated for the next lattice element. By this means, we are able to calculate the IBS growth rate utilizing a macroparticle approach.

B. Compton scattering and the 3D algorithm

The interaction between laser photon and electron beam can be considered as a cooling effect in the transverse direction [15]. When the CS alone takes effect in beam dynamics, the partial equilibrium transverse emittance and energy spread are [16]

$$\epsilon_{x,y0} = \frac{\beta_{x,y}E_{\text{las}}}{3E_e} \quad (11)$$

$$\sigma_{\delta 0}^2 = \frac{\gamma^2 E_{\text{las}}}{3E_e}, \quad (12)$$

where E_e is the energy of the electron beam.

Utilizing the parameters in Table III, we obtained $\epsilon_{x,y0} = 5\times10^{-10}$ m and $\sigma_{\delta 0} = 1\%$. Since the initial emittance and energy spread of the electron beam are $\epsilon_{x,y} = 2\times10^{-8}$ m and $\sigma_\delta = 0.2\%$, we can foresee that, as the IBS pushes the emittance further away from the partial equilibrium emittance, the cooling effect of the CS will benefit the transverse emittance throughout the storage period. With respect to the longitudinal direction, the CS will contribute to the energy spread [16]. This conclusion will be demonstrated in the simulation later (see Sec. IV).

In the CS simulation, we mainly followed the approaches of CAIN [17–19]. We will briefly review the algorithm applied in the 3D simulation code (see Ref. [18] for more details).

In the rest frame of the electron, for an x-ray photon scattered by the electron, the polar scattering angle of the photon θ can be represented by

$$\cos\theta = 1 - \frac{2(e^z - 1)}{\lambda}, \quad (13)$$

where $z = \log(\omega/\omega')$, ω and ω' represent the photon

TABLE III. Parameters of the electron beam, laser pulse, and their interaction.

Parameters	Value
Electron	
Energy, MeV	50
Beam charge, nC	1
Transverse emittance, m	2×10^{-8}
Energy spread	0.2%
Beam pulse length, ps	10
Laser	
Pulse energy, mJ	1–100
Laser photon wavelength, nm	800
Rayleigh length, mm	6
Pulse length, fs	100
Spot size at IP, μm	20
Collision angle	0°
Maximum scattered photon energy, keV	56.4
Scattered photon pulse length, ps	10
Peak intensity, phot/s	4.5×10^{12}

energies before and after the collision, respectively, and $\lambda = 2\omega/m$, m is the mass of the electron.

The differential cross section of CS can be described by

$$\frac{d\sigma}{d\bar{z}} = 4\pi r_0^2 \frac{L_\lambda}{\lambda} F(\bar{z}) \tag{14}$$

$$F(\bar{z}) = \frac{1}{2L_\lambda}[1 + e^{-2z} - e^{-z}\sin^2\theta - h\cos\theta(1 - e^{-2z})], \tag{15}$$

where $L_\lambda = \log(1+\lambda)$, $\bar{z} = \frac{z}{L_\lambda}$, $h = \frac{\vec{k}}{\omega} \cdot \vec{\zeta}\vec{\xi}_2^{(L)}$, $\vec{k}$ is the initial momentum of photon, $\vec{\zeta}$ is the polarization vector of the electron, and $\vec{\xi}$ is the initial Stokes parameters of photon.

The integral cross section is given by

$$\sigma_{\text{total}} = 4\pi r_0^2 \frac{L_\lambda}{\lambda} F_{\text{int}}(\lambda), \tag{16}$$

where

$$F_{\text{int}}(\lambda) = \frac{1}{2L_\lambda}\left\{\left(1 - \frac{4}{\lambda} - \frac{8}{\lambda^2}\right)L_\lambda + \frac{1}{2} + \frac{8}{\lambda} - \frac{1}{2(1+\lambda)^2} + h\left[-\left(1 + \frac{2}{\lambda}\right)L_\lambda + 2 + \frac{1}{2(1+\lambda)^2}\right]\right\}. \tag{17}$$

The energy of the scattered photon can be evaluated by

$$\frac{1}{\omega'} - \frac{1}{\omega} = \frac{1 - \cos\theta}{m}. \tag{18}$$

The azimuthal angle ϕ of the scattered photon follows the distribution

$$f(\phi) = 1 + A_1\cos\phi + B_1\sin\phi + A_2\cos2\phi + B_2\sin2\phi, \tag{19}$$

where

$$A_1 = u_1 \cdot \vec{m} \times \vec{n} \cdot \vec{\zeta} \tag{20}$$

$$B_1 = u_1 \cdot \vec{m} \cdot \vec{\zeta} \tag{21}$$

$$A_2 = u_2(\xi_1 \sin2\alpha + \xi_3 \cos2\alpha) \tag{22}$$

$$B_2 = u_2(\xi_1 \cos2\alpha - \xi_3 \sin2\alpha) \tag{23}$$

$$\vec{m} = -\vec{i}\sin\alpha + \vec{j}\cos\alpha \tag{24}$$

$$u_1 = -\frac{\lambda}{2}\frac{(1-\cos\theta)\sin\theta}{F_0 e^{2z}}\xi_2 \qquad u_2 = -\frac{\sin^2\theta}{F_0 e^z}\xi_1 \tag{25}$$

$$F_0 = e^{-z} + e^z - \sin^2\theta - h(e^{-z} + e^z)\cos\theta, \tag{26}$$

where α is the angle between $\vec{k}$ and $\vec{e}_1$ on the plane of $\vec{e}_1$ and $\vec{e}_2$; $\vec{n}$ is the unit vector in the direction of propagation of the electron; $\vec{e}_1$ and $\vec{e}_2$ are the basis vectors for the photon polarization, which are perpendicular to $\vec{k}$; $\vec{i}$ and $\vec{j}$ are the basis vectors for the electron polarization, which are perpendicular to $\vec{n}$.

The algorithm of the CS simulation can be summarized in this way. For each macroparticle that goes into the CS module, the strength of the laser energy is calculated for each time step. The scattering chance for the macroparticle is determined by Eq. (16). For the macroparticle that scatters off an x-ray photon, $\bar{z}$ is generated according to the distribution defined in Eq. (15); the polar angle θ is calculated according to Eq. (13); and the scattered photon energy ω' is calculated by Eq. (18); the azimuthal angle ϕ can be generated according to Eq. (19). With these parameters calculated, we obtained the 3D information of the scattered photon.

C. Coherent synchrotron radiation

Since the LESR utilizes electron beam of 10 ps and charge quantity of 1 nC, and bending radius of about 0.4 m, the coherent synchrotron radiation (CSR) may alone account for the dynamic instability. Utilizing the approaches of Venturini, Warnock, and co-workers [5,6], we obtained the CSR threshold at $Q_{\text{th}} = 20$ nC with parameters presented in Table III (see Sec. V A of Ref. [5] for more details). Hence, for our current design, the LESR operates below the CSR instability threshold.

IV. PARAMETERS OF THE BEAM AND THE SCATTERED PHOTON

With the laser energy 1 mJ stored in the optical cavity and the electron energy of 50 MeV, one can generate the x-ray pulse with the peak intensity of 4.5×10^{12} phot/s. We assumed a head-on collision in the simulation. The main

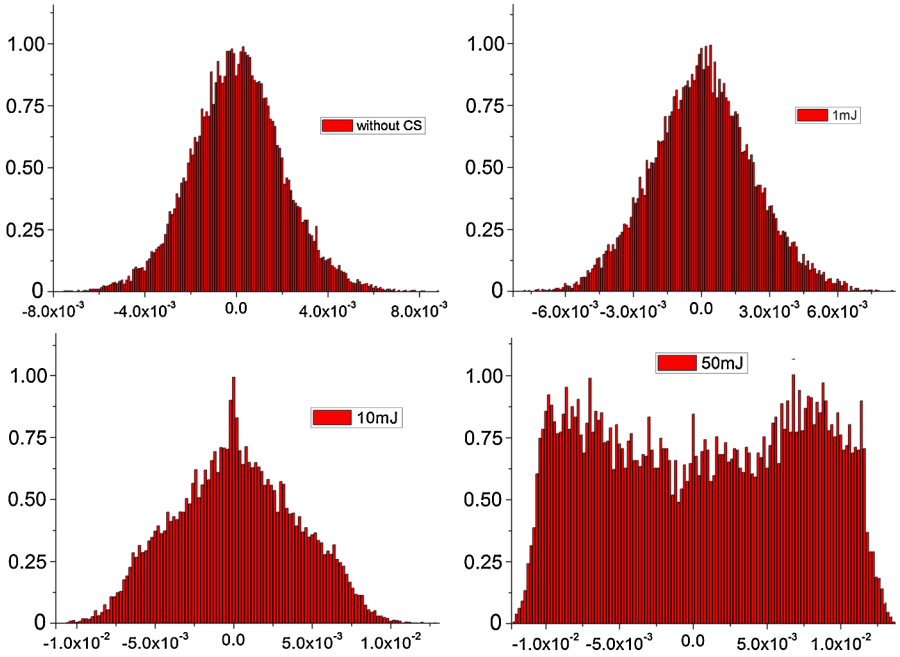

FIG. 5. (Color) The normalized longitudinal momentum distributions of the electron beam at 200 000 turns of the storage period. The stored laser energy is 0, 1, 10, and 50 mJ.

parameters we utilized in the simulation are listed in Table III.

A. Longitudinal distribution of the electron beam

The normalized longitudinal momentum distributions of the electron beam at 200 000 turns of its storage period with the laser energy of 0, 1, 10, and 50 mJ stored in the optical cavity are shown in Fig. 5. The figure shows that, as laser energy becomes stronger, the energy distribution may be different from the Gaussian distribution. Nevertheless, since we adopted macroparticle algorithms in our simulation, the code is adequate for the electron beam with an arbitrary distribution.

B. Emittance growth of the electron beam

The emittance growth of the electron beam is presented in Fig. 6. The IBS is the dominant factor in the transverse direction, while IBS and CS contribute to the longitudinal direction. We partly suppressed the IBS growth rate by reducing the $\mathcal{H}_x$ function as mentioned in Sec. II. However, there is still a ten-time growth in the horizontal emittance and a 40% growth in the energy spread (stored laser energy 1 mJ). We can see that, by increasing the laser energy, the horizontal emittance growth rate decreases while the energy spread growth rate increases. This is evident in the conclusion in Sec. III that as stored laser energy becomes stronger, the cooling effect of the CS becomes more obvious, while the energy spread increases more rapidly. The growth in energy spread leads to a growth in the beam length, which indicates a growth in the x-ray pulse length.

C. Spatial distribution and spectrum of the scattered photon

Figure 7 presents the 2D spatial distributions of the scattered photon number in a CCD placed 1.5 meters away from the IP. The laser energy is 1, 10, and 50 mJ. In Fig. 7, the subfigures in column (a) are the photons accumulated in the first 100 000 turns, while the subfigures in column (b) are the photons accumulated in the last 100 000 turns. The normalized spatial distributions of the scattered photon intensity are shown in column (c). We

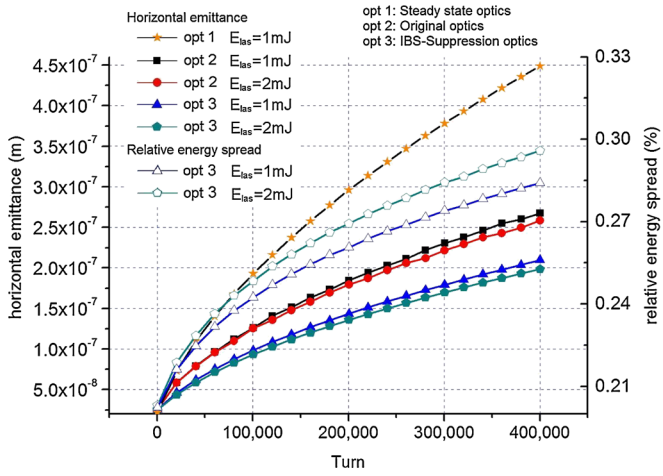

FIG. 6. (Color) The emittance growth and energy spread for the original optics [7], the IBS-suppression optics, and the steady mode optics [22]. As shown in the figure, CS plays as a cooling effect in the transverse direction while contributing to the growth of the energy spread.

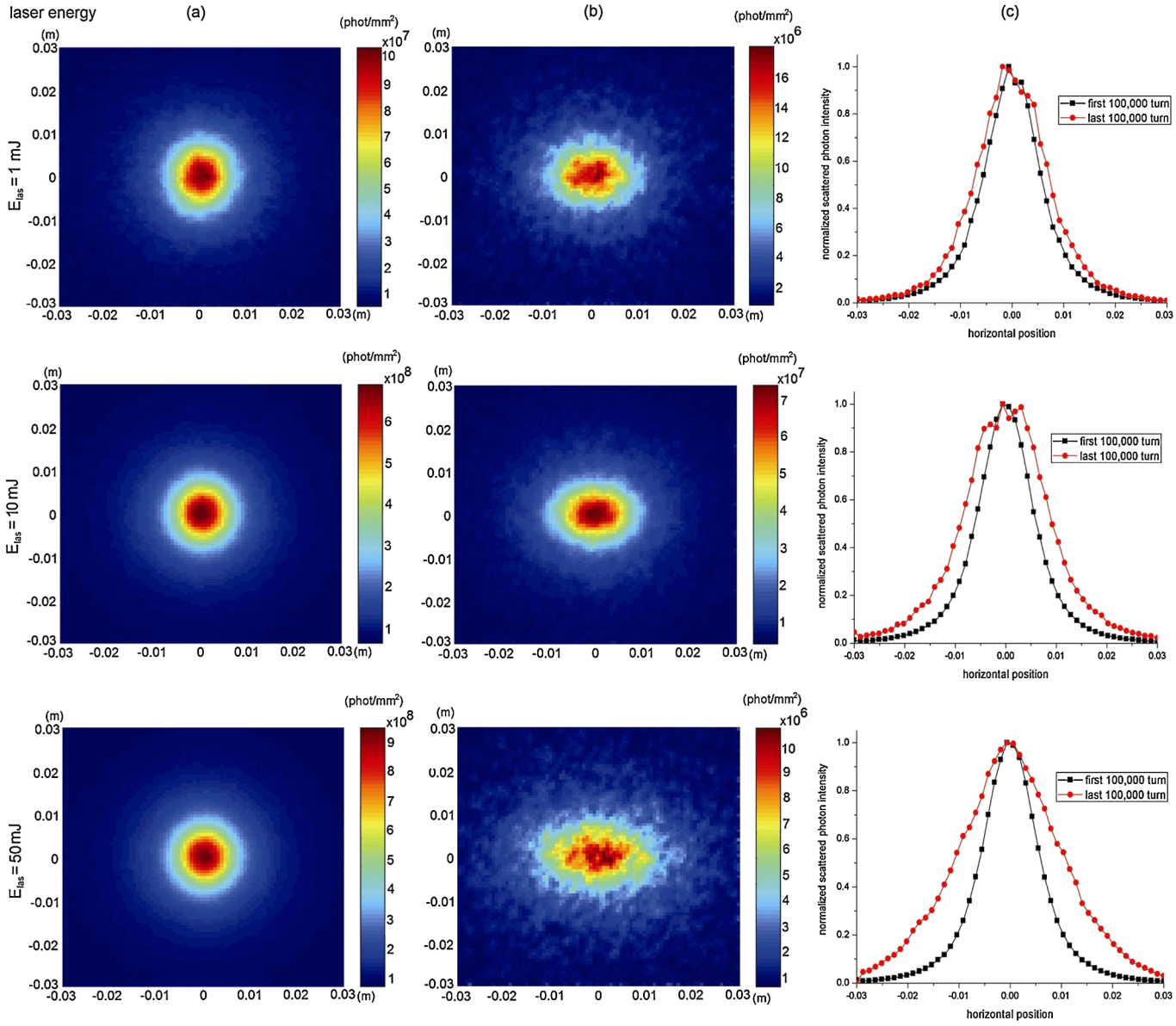

FIG. 7. (Color) The spatial distributions of the x-ray photon in the CCD placed 1.5 m away from the IP with different laser energies. The subfigures in column (a) are the spatial distributions of the x-ray photon intensity for the first 100 000 turns; subfigures in column (b) are those for the last 100 000 turns. The subfigures in column (c) are the normalized spatial distributions of the photon intensity for the first and last 100 000 turns. The growth in the light spot horizontal size indicates the growth in horizontal emittance of the electron beam.

integrated the vertical direction to show the growth in the horizontal sizes of the distributions. As presented in the figure, the maximum number of photons per mm^2 decreases quite rapidly. The horizontal sizes of the light spots in column (a) are smaller than those in column (b). Likewise, the FWHM of the normalized distributions of the last 100 000 turns is larger than those of the first 100 000 turns. The reason is that the photons are drifted to the CCD 1.5 meters away from the IP; therefore, the spatial distribution presented in the CCD is mainly determined by the scattering angle of the x-ray photon rather than its spatial position where it is generated. Since the photon scattering angle reveals the polar angle of the electron velocity, the growth in the light spot horizontal size is attributable to the horizontal emittance growth of the electron beam.

The scattered photon spectrums at different positions for the laser energy of 1 mJ are presented in Fig. 8. To identify the spatial difference of the spectrums, we calculated the spectrum at the horizontal position of 0, 1, and 2 cm. The figure shows that in the center of the CCD the peak of the spectrum exists at the high energy section. As it goes farther from the center, the peak of the spectrum moves toward the low-energy section. This is obvious because the

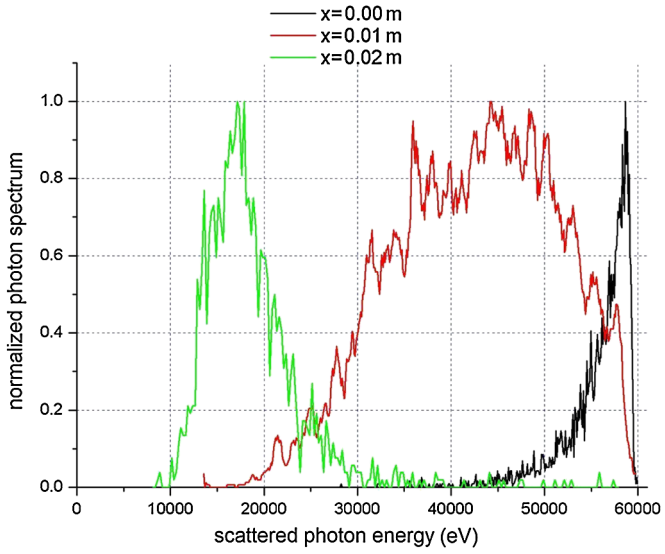

FIG. 8. (Color) Spectrums of the photon energy at $x = 0$, 1, and 2 cm. We can see that at different positions of the CCD, we have different spectrums. The farther away the point is from the center, the lower the peak of the spectrum. This result is consistent with the analytical result in Eq. (13).

energy of the photons is related to the polar scattering angle as indicated in Eq. (13): the larger the polar scattering angle, the smaller the scattered photon energy.

The average value of the x-ray photon yield is 3×10^{12} phot/s, and the number of photons within the scattering angle 1 mrad is 5×10^{10} phot/s with an FWHM spectrum width of 10%. These parameters meet the requirements for biological and medical applications.

D. Temporal distribution of the total photon yield

The temporal distribution of the scattered photon yield for the laser energy of 1 mJ is presented in Fig. 9. We can see that the photon yield decreases to 40% of the initial value. This is quite obvious because the beam size grows in all three directions in the storage period, which reduces the electron density. We compared this full Monte Carlo result with that of the analytical result [20],

$$N_x = \frac{\sigma_{\text{total}} N_e N_\gamma}{2\pi\sqrt{\sigma_{ey}^2 + \sigma_{ly}^2}} \times \frac{1}{\sqrt{(\sigma_{ex}^2 + \sigma_{lx}^2)\cos^2(\alpha/2) + (\sigma_{es}^2 + \sigma_{ls}^2)\sin^2(\alpha/2)}}, \tag{27}$$

where σ_{ex}, σ_{lx}, σ_{ey}, σ_{ly}, σ_{ez}, and σ_{lz} are the transverse and longitudinal sizes of beam and laser pulse, respectively; N_e and N_γ are the number of electrons and the number of laser photons in a single pulse, respectively; α is the collision angle, with $\alpha = 0$ corresponding to the head-on collision, and σ_{total} is the CS cross section. We

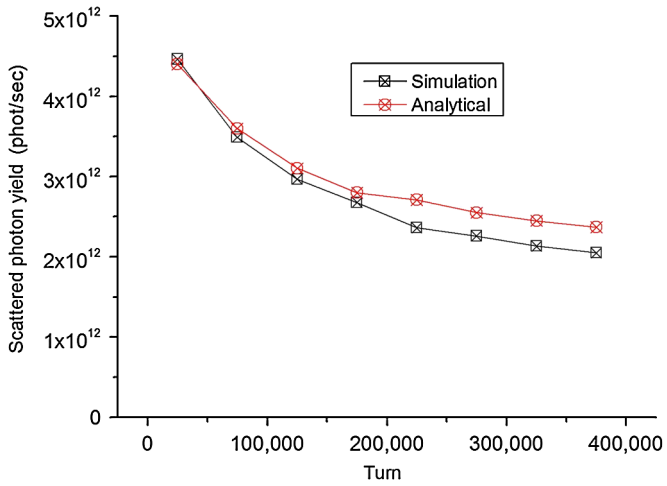

FIG. 9. (Color) The temporal distribution of the total yield of the x-ray photons. We compared the simulation result with that of the analytical one, and they agree well with each other. Owing to the strong IBS effect, the total yield decreases to about 40% of the value at the startup.

can see that the simulation result agrees well with the analytical one.

V. CONCLUSIONS AND DISCUSSIONS

We proposed a lattice for the pulse mode of the LESR. Utilizing the IBS-suppression scheme, the new optics achieves 25% reduction in the IBS growth rate compared with the original optics. We adopted the binary collision model to calculate the IBS growth rate in our algorithm. Compton scattering is simulated using a full 3D simulation code, which gave us a detailed analysis of the spatial and temporal distribution of the scattered photon yield as well as its influence on the electron. With respect to coherent synchrotron radiation, we obtained the instability threshold of $Q_{\text{th}} = 20$ nC utilizing the approaches in Refs. [5,6].

By reducing the value of the $\mathcal{H}_x$ and beta function around the ring, we can suppress the emittance growth and tune shift owing to space charge. However, the decrease in x-ray photon quality due to the IBS is inevitable at the state-of-the-art technique. Owing to the electron beam emittance growth, the scattered photon yield decreases while the scattered photon pulse length increases. We likewise witnessed growth in the light spot horizontal size owing to the emittance growth of the electron beam.

In such a compact storage ring, the fringe fields of the magnets can affect the beam dynamics. The Twiss function and frequency map can be changed if we apply realistic fringe fields in the simulation. Moreover, since the injection system is placed closely to the bending magnet, the fringe field of the bending magnet can affect the injection stability [21]. Furthermore, the CSR effect should be further studied utilizing more sophisticated approaches. We believe that these issues should be investigated in future work to justify the feasibility of the LESR lattice design.

ACKNOWLEDGMENTS

The authors are greatly in debt to Dr. P. Gladkikh of NSC KIPT and Dr. Q. Qin of IHEP for helpful discussions on lattice design. We would also like to thank Dr. L. Nadolski of SOLEIL and Dr. Yi Jiao of IHEP for helpful discussions on frequency map analysis, and Dr. B. Nash and Dr. Jie Wei for fruitful discussions on the IBS theory. This work was supported by the Chinese National Foundation of Natural Sciences under Contract No. 10735050.

APPENDIX

In the following, we will demonstrate that with the azimuthal angle ϕ distributes uniformly in $[0, 2\pi]$ and the equivalent polar angle φ in Eq. (10), the invariant changes caused by the binary collision are the same as those in Eqs. (7)–(9) for the time interval Δt_s.

For two colliding particles, the momentum changes for particle 1 can be expressed by Eqs. (4)–(6). For the transverse direction, averaging over the azimuthal angle ϕ in Eq. (4), we obtain

$$\frac{\langle \Delta P_x \rangle}{P} = \frac{1}{4\pi}\int_0^{2\pi}\left\{\left[\zeta\sqrt{1+\frac{\xi^2}{4\alpha^2}}\sin\phi - \frac{\xi\theta}{2\alpha}\cos\phi\right]\sin\varphi + \theta(\cos\varphi - 1)\right\}d\phi = -\theta\sin^2\frac{\varphi}{2} \approx -\frac{\theta\varphi^2}{4} \quad \text{(A1)}$$

and

$$\begin{aligned}\frac{\langle \Delta P_x^2 \rangle}{P^2} &= \frac{1}{8\pi}\int_0^{2\pi}\left\{\left[\zeta\sqrt{1+\frac{\xi^2}{4\alpha^2}}\sin\phi - \frac{\xi\theta}{2\alpha}\cos\phi\right]\sin\varphi + \theta(\cos\varphi - 1)\right\}^2 d\phi \\ &= \frac{1}{8}\left\{\left[\zeta^2\left(1+\frac{\xi^2}{4\alpha^2}\right) + \frac{\xi^2\theta^2}{4\alpha^2}\right]\sin^2\varphi + \theta^2(\cos\varphi - 1)^2\right\}. \end{aligned} \quad \text{(A2)}$$

Taking into account $4\alpha^2 = \theta^2 + \zeta^2$, and dropping the term $\theta^2(\cos\varphi - 1)^2$ which is relatively small, we have

$$\frac{\langle \Delta P_x^2 \rangle}{P^2} \approx \frac{\varphi^2}{8}(\xi^2 + \zeta^2). \quad \text{(A3)}$$

Correspondingly, we have

$$\frac{\langle \Delta P_y \rangle}{P} \approx -\frac{\zeta\varphi^2}{4} \quad \text{(A4)}$$

$$\frac{\langle \Delta P_y^2 \rangle}{P^2} \approx \frac{\varphi^2}{8}(\xi^2 + \theta^2) \quad \text{(A5)}$$

$$\frac{\langle \Delta P_s \rangle}{P} \approx -\frac{\gamma\xi\varphi^2}{4} \quad \text{(A6)}$$

$$\frac{\langle \Delta P_s^2 \rangle}{P^2} \approx \frac{\gamma^2\varphi^2}{8}(\zeta^2 + \theta^2). \quad \text{(A7)}$$

Meanwhile, the invariant changes of the particle owing to its momentum changes in a storage ring are [14]

$$\Delta J_{1x} = x_1'\frac{\Delta P_x}{P} + \frac{1}{2}\left(\frac{\Delta P_x}{P}\right)^2 - \frac{x_{\beta 1}}{\beta_x^2}D_x\frac{\Delta P_s}{P} + \frac{D_x^2}{2\beta_x^2}\left(\frac{\Delta P_s}{P}\right)^2 \quad \text{(A8)}$$

$$\Delta J_{1y} = y_1'\frac{\Delta P_y}{P} + \frac{1}{2}\left(\frac{\Delta P_y}{P}\right)^2 \quad \text{(A9)}$$

$$\Delta J_{1s} = \delta_1\frac{\Delta P_s}{P} + \frac{1}{2}\left(\frac{\Delta P_s}{P}\right)^2. \quad \text{(A10)}$$

Taking the horizontal direction for instance, by substituting φ with Eq. (10), and replacing $\frac{\Delta P_x}{P}$, $(\frac{\Delta P_x}{P})^2$, $\frac{\Delta P_s}{P}$, and $(\frac{\Delta P_s}{P})^2$ in Eq. (A8) with Eqs. (A1), (A3), (A6), and (A7), we finally obtained

$$\frac{\Delta J_{1x}}{\Delta t_s} = \frac{\pi r_0^2}{4\gamma^2\bar{\beta}^3}c\rho L_c\left[-4x_1'\theta + \xi^2 + \zeta^2 + 4\frac{x_{\beta 1}D_x}{\beta_x^2}\gamma\xi + \frac{D_x^2\gamma^2}{\beta_x^2}(\theta^2 + \zeta^2)\right] \quad \text{(A11)}$$

which is the same as in Eq. (7). The other two invariants can be generated in this way correspondingly. Hence, we proved that the discrete random process provides the same emittance growth rate as that of the IBS effect in the time interval Δt_s.

[1] Z. Huang and R. D. Ruth, Phys. Rev. Lett. **80**, 976 (1998).
[2] P. Gladkikh, Phys. Rev. ST Accel. Beams **8**, 050702 (2005).
[3] R. J. Loewen, Ph.D. thesis, Stanford, 2003.
[4] N. Alekseev, A. Bolshakov, E. Mustafin, and P. Zenkevich, in *Space Charge Dominated Beam Physics for Heavy Ion Fusion*, edited by Y. K. Batygin (AIP, New York, 1999), Vol. 480, pp. 31–41.
[5] M. Venturini, R. Warnock, R. Ruth, and J. Ellison, Phys. Rev. ST Accel. Beams **8**, 014202 (2005).
[6] R. Warnock, R. Ruth, M. Venturini, and J. Ellison, Phys. Rev. ST Accel. Beams **8**, 014402 (2005).
[7] P. Yu, Y. Wang, and W. Huang, in *Proceedings of the 11th European Particle Accelerator Conference, Genoa, 2008* (EPS-AG, Genoa, Italy, 2008), pp. 187–189, http://accelconf.web.cern.ch/AccelConf/e08/papers/mopc053.pdf.
[8] V. Litvinenko *et al.*, in Proceedings of the 11th European Particle Accelerator Conference, Genoa, 2008, Ref. [7], pp. 2557–2559, http://accelconf.web.cern.ch/AccelConf/e08/papers/wepp015.pdf.
[9] J. Le Duff, CERN Report No. CERN 95-06, 1995, pp. 573–586.

[10] This optics is designed for the steady mode of the LESR that utilizes the same lattice as the pulse mode. See Ref. [22] for more details.
[11] H. Wiedemann, *Particle Accelerator Physics* (Springer, Berlin, 1999).
[12] A. Streun, course given at CERN accelerator school, Benodet (1999).
[13] L. Nadolski and J. Laskar, Phys. Rev. ST Accel. Beams **6**, 114801 (2003).
[14] A. Piwinski, Lect. Notes Phys. **296**, 297 (1988).
[15] V. Telnov, Phys. Rev. Lett. **78**, 4757 (1997).
[16] E. Bulyak and V. Skomorokhov, in *Proceedings of the 9th European Particle Accelerator Conference, Lucerne, 2004* (EPS-AG, Lucerne, Switzerland, 2004), pp. 2409–2411, http://accelconf.web.cern.ch/accelconf/e04/papers/weplt138.pdf.
[17] P. Chen, T. Ohgaki, A. Spitkovsky, T. Takahashi, and K. Yokoya, Nucl. Instrum. Methods Phys. Res., Sect. A **397**, 458 (1997).
[18] K. Yokoya, Users Manual of CAIN (2003), Version 2.35.
[19] V. Berestetskii, E. Lifshitz, and L. Pitaevskii, *Quantum Electrodynamics* (Pergamon Press, Oxford, 1982).
[20] J. Yang, M. Washio, A. Endo, and T. Hori, Nucl. Instrum. Methods Phys. Res., Sect. A **428**, 556 (1999).
[21] A. O. Mytsykov, P. I. Gladkikh, O. V. Ryezayev, and A. Y. Zelinsky, in Proceedings of the 9th European Particle Accelerator Conference, Lucerne, 2004, Ref. [16], pp. 1434–1436, http://cern.ch/accelconf/e04/papers/tuplt132.pdf.
[22] P. Yu *et al.*, Chinese Phys. C (to be published).